

Clarifying ambiguity in intraseasonal Southern Hemisphere climate modes during austral winter

N. Joss Matthewman¹ and Gudrun Magnusdottir¹

Received 10 August 2011; revised 18 October 2011; accepted 22 November 2011; published 1 February 2012.

[1] The relative importance of annular and nonannular characteristics in the wintertime Southern Hemisphere circulation is investigated using reanalysis data between 1978 and 2010. Weekly averaged data are chosen to capture the typically short time scale of intraseasonal atmospheric variability. In existing studies, the southern annular mode (SAM) has been shown to exhibit significant nonannular behavior in the western Southern Hemisphere during austral winter. Variability in this region is also characterized by wave-like disturbances, and this “overlap” in nonannular behavior between different climate modes has led to a lack of consensus when defining and measuring impact from these wave-like disturbances. A number of approaches are adopted, including empirical orthogonal function analysis, teleconnection correlation analysis, and the application of a vector autoregression model to isolate directions of causality and wave propagation. Austral winter variability is shown to be dominated by nonannular wave-like disturbances, rather than a seesaw pattern between high and middle latitudes. The wave-like disturbances have the largest amplitude in the western Southern Hemisphere, are quasi-stationary, and exhibit eastward propagation of information. This suggests that the dominant pattern of western Southern Hemisphere intraseasonal variability during austral winter, which is commonly associated with the SAM, is, in fact, a wave-like mode of variability.

Citation: Matthewman, N. J., and G. Magnusdottir (2012), Clarifying ambiguity in intraseasonal Southern Hemisphere climate modes during austral winter, *J. Geophys. Res.*, 117, D03105, doi:10.1029/2011JD016707.

1. Introduction

[2] Despite a general interest in the annular mode paradigm when describing extratropical variability in both hemispheres [e.g., *Gong and Wang*, 1999; *Thompson and Wallace*, 1998], a nonannular or regional approach may be more suited to accurately capturing variability in some seasons [e.g., *Ambaum et al.*, 2001]. One argument is that extratropical variability in different regions of a given hemisphere, which under the annular paradigm should be linked via their shared high-latitude center of action, are often not significantly correlated with one another [e.g., *Ambaum et al.*, 2001]. Another study comparing the relative importance of annular and nonannular characteristics in both hemispheres is that of *Cohen and Saito* [2002]. Using cluster analysis of various leading empirical orthogonal function (EOF) modes, they found that atmospheric anomalies in the lower troposphere are strongly nonannular in the Northern Hemisphere during boreal winter (December–January–February), and weakly nonannular in the Southern Hemisphere during austral spring (November).

[3] Prominent modes of Southern Hemisphere intraseasonal extratropical variability other than the southern annular mode (SAM) are the Pacific South American (PSA) pattern in the western Southern Hemisphere, and quasi-stationary zonal wave number 3, 4, and 5 disturbances, all of which exhibit wave-like characteristics. The definition of these modes is surprisingly inconsistent across the literature, although authors seem to agree upon some common characteristics, including a tropically forced quasi-stationary wave pattern in the western Southern Hemisphere [*Berbery et al.*, 1992; *Frederiksen and Zheng*, 2007; *Hobbs and Raphael*, 2010a; *Mo and Paegle*, 2001; *Yuan and Li*, 2008].

[4] While the quasi-stationary zonal waves can be thought of in terms of their respective Fourier modes, the definition of the PSA is somewhat less rigid, although it has often been defined in terms of nonleading order hemispheric EOF modes which exhibit wave-like patterns in the western Southern Hemisphere [e.g., *Kidson*, 1999; *Mo and Paegle*, 2001]. One particular approach, which has been popular in several studies [e.g., *Hobbs and Raphael*, 2010a; *Mo and Paegle*, 2001], involves partitioning the PSA into two quasi-independent modes, PSA 1 and PSA 2 using hemispheric EOFs 2 and 3, respectively, with both PSA modes exhibiting combined zonal wave number 3 and wave number 1 characteristics. However, this definition of the PSA has somewhat undesirable properties. First, one must be careful when attributing a direct correspondence between EOF modes, particularly higher-order modes, and

¹Department of Earth System Science, University of California, Irvine, California, USA.

observed modes of climate variability [Ambeam *et al.*, 2001; Hannachi *et al.*, 2007; Monahan *et al.*, 2009]. Second, to our knowledge, in all such studies EOFs 2 and 3 are not well separated from one another (e.g., following the criterion of North *et al.* [1982]), which raises the question of whether the PSA 1 and PSA 2 climate modes are truly independent. As an alternative, Yuan and Li [2008] suggest using a fixed point index method to define the PSA, similar to that suggested by Wallace and Gutzler [1981] for the Pacific North American pattern. Following this approach, they identify three alternating pressure anomaly centers located east of New Zealand, over the Bellingshausen Sea, and east of South America, which when combined give an index measuring the overall strength and sign of this peak-trough-peak pattern.

[5] All of these modes, the SAM, the PSA, and the Fourier mode zonal wave patterns, have been shown to exhibit a degree of seasonality. For example, in their intraseasonal study, Mo and Paegle [2001] found that circumpolar Rossby waves have a slow phase velocity in austral winter, while being largely stationary in austral summer. These waves can be thought of as being related to either the PSA or Fourier zonal wave patterns. Similarly, although described as being annular, the SAM exhibits zonal wave number 3 characteristics in austral winter. It is the prominent zonal wave number 3 pattern, which is often interpreted as the SAM, that we are interested in.

[6] The wave number 3 component of the SAM is most prominent in the western Southern Hemisphere. Therefore, in austral winter the overlapping existence of the PSA and quasi-stationary zonal wave number 3 modes is made even more ambiguous by their collocation with the SAM in the Pacific sector. An example of this is given by Hobbs and Raphael [2010a], who found that the Yuan and Li [2008] PSA centers of action coincided almost exactly with the wave number 3 component of the wintertime SAM. Hobbs and Raphael therefore rejected the Yuan and Li [2008] PSA definition in favor of the EOF 2 and 3 definition of Mo and Paegle [2001]. However, this raises an interesting question: how appropriate is the annular mode paradigm in the western Southern Hemisphere during austral winter? Is it possible that the wave number 3 pattern which dominates this portion of the SAM has been misidentified, and is in fact a signature of the PSA or some other nonannular mode? While the nonannular nature of the Southern Hemisphere tropospheric circulation has been noted before [e.g., Cohen and Saito, 2002], our objective here is to revisit the problem using a number of techniques, to understand the ambiguity of the wintertime PSA and SAM. Given the impact that these modes have on regional climate, for example precipitation over South America and Australia [Hendon *et al.*, 2007; Mo and Paegle, 2001], or sea ice variability in the Southern Ocean [Hobbs and Raphael, 2010b; Yuan and Li, 2008], it is desirable to address such ambiguity if one is to attribute regional climate impacts to the appropriate climate mode.

[7] The manuscript will proceed as follows. In section 2 we introduce the intraseasonal data used in our study. Section 3 then introduces each of the techniques used to analyze these data: EOF analysis, zonal and meridional winds, the Wallace and Gutzler [1981] teleconnection method, and two vector autoregressive model applications.

Section 4 presents our results, and a summary of our conclusions appears in section 5.

2. Data Sets

[8] Data are taken from the National Centers for Environmental Prediction–National Centers for Atmospheric Research (NCEP–NCAR) reanalysis data set from 1978 onward. We use geopotential height on the 700 hPa pressure surface, and horizontal wind (u, v) on the 500 hPa pressure surface. As the Southern Hemisphere troposphere is characterized by an equivalent barotropic structure, these pressure surfaces are taken to be representative of the behavior of the respective fields at all heights (although not shown, this was confirmed by repeating our analysis at different heights throughout the troposphere). Weekly averaging is performed on all data for weeks starting 1 January 1978 up to 24 December 2010, with weeks being grouped into two seasonal bins: January–February–March (weeks starting 1 January up to 26 March), corresponding to austral summer, and July–August–September (weeks starting 2 July up to 24 September), corresponding to austral winter. It has been noted in previous studies [e.g., Bromwich and Fogt, 2004] that the NCEP–NCAR data set exhibits spurious biases in atmospheric fields in the Southern Hemisphere, especially in austral nonsummer months. However, the fact that these biases decrease with height, that the NCEP–NCAR reanalysis continuously covers our time period of interest, and the prevalence of NCEP–NCAR data in existing studies, makes this data set the best candidate for our choice of analysis. When working with 700 hPa geopotential height data, the 1978–2010 linear trend is removed from each seasonal bin individually, and the 1978–2010 weekly mean is removed from each week in turn, giving detrended and deseasonalized geopotential height anomaly field z (or B when referring to the value at a given base point, as discussed in section 3.3).

3. Methodology

3.1. EOF Analysis

[9] Seasonal patterns of variability in z are identified using empirical orthogonal function analysis on the detrended and deseasonalized seasonally binned weekly averaged data, using latitudes 20° – 80° S and all longitudes. When constructing the EOFs, z data are weighted by cosine of latitude, to ensure that data points near the pole do not have a disproportionate impact on the analysis.

3.2. Zonal and Meridional Winds

[10] We analyze the zonal and meridional components of the wind at each location in the domain by constructing a seasonal average of the weekly average wind magnitude

$$\overline{|u(\lambda, \phi)|}_{\text{weekly}}^{\text{season}} = \frac{1}{T} \sum_{t=1}^T |u(\lambda, \phi, t)|_{\text{weekly}}, \quad (1)$$

$$\overline{|v(\lambda, \phi)|}_{\text{weekly}}^{\text{season}} = \frac{1}{T} \sum_{t=1}^T |v(\lambda, \phi, t)|_{\text{weekly}}, \quad (2)$$

Table 1. The Three Types of Vector Autoregressive Models and Their Corresponding Restrictions on Equations (6) and (7)

Model	Symbol	Restriction	Description
Unrestricted	U	none	fully coupled model
Restricted 1	R1	$a_{12} \equiv 0$	B_t is independent of z_{t-1}
Restricted 2	R2	$a_{21} \equiv 0$	z_t is independent of B_{t-1}

where T is the number of weekly observations in a given season over all available years, and the overbar denotes the average over all such observations. The absolute value is used to avoid cancellation of large opposite signed values, which is particularly important in the case of the meridional wind.

3.3. Correlation Analysis

[11] An alternative approach to EOF analysis is the teleconnection method of *Wallace and Gutzler* [1981], who employ a map-based point correlation analysis to isolate regions in the Northern Hemisphere which are associated with a strong negative correlation elsewhere in the domain. This approach, or variations thereof, has also been employed in the Southern Hemisphere [*Ambrizzi et al.*, 1995; *Berbery et al.*, 1992], and is briefly summarized as follows. Given any choice of base point (λ_B, ϕ_B) in the 20° – 80° S annular domain, and denoting the geopotential height anomaly at this point as $B = z(\lambda_B, \phi_B)$, we calculate a contemporaneous correlation map between B and all other z throughout the domain using

$$r_B(\lambda, \phi) = \text{corr}[B, z(\lambda, \phi)]. \quad (3)$$

[12] The teleconnectivity value F_B at this base point is then the absolute value of the strongest negative contemporaneous correlation in r_B

$$F_B = |\min\{r_B(\lambda, \phi)\}|. \quad (4)$$

[13] By repeating this process for every base point within the domain, we build the teleconnection map $\mathcal{T}(\lambda_B, \phi_B)$, as a function of longitude and latitude:

$$\mathcal{T}(\lambda_B, \phi_B) = \{F_B; 0 \leq \lambda_B < 360, -80 \leq \phi_B \leq -20\}. \quad (5)$$

3.4. Vector Autoregressive Model Framework and Hypothesis Testing

[14] When considering teleconnective relationships between geopotential height anomalies at two different locations, we test causality using a vector autoregressive (VAR) model, which has been used in the context of climate variability in several recent studies [*Matthewman and Magnusdottir*, 2011; *Mosedale et al.*, 2006; *Strong et al.*, 2009].

[15] In the VAR model, at time t , geopotential height anomalies at a specified base point, B_t , and at some other “test location” in the domain, z_t , are related to their previous values using

$$B_t = a_{11}B_{t-1} + a_{12}z_{t-1} + \epsilon_t^B \quad (6)$$

$$z_t = a_{21}B_{t-1} + a_{22}z_{t-1} + \epsilon_t^z. \quad (7)$$

[16] In equations (6) and (7), subscript t denotes a given time in the B and z time series, and the coefficients (a_{ij}) control lagged dependence of B and z on their values in the

preceding week. White noise stochastic forcing terms, ϵ_t^B and ϵ_t^z , represent random fluctuations in B and z not accounted for by the autoregressive component of the model. They have distinct variances σ_B^2 and σ_z^2 . Given a particular choice of base point and test location, with their respective geopotential height time series B and z , the VAR model parameters a_{ij} , σ_B^2 , and σ_z^2 are estimated by fitting (6) and (7) to observed B and z time series, as described in Appendix A.

[17] The main objective of applying the VAR model is to identify directions of Granger causality [*Granger*, 1969]. For example, if z Granger causes B (denoted $z \Rightarrow B$), then a VAR model in which B_t depends on z_{t-1} (in addition to B_{t-1}) is a significantly better fit to observed data than a model in which B_t only depends on B_{t-1} and not on z_{t-1} . Therefore, the VAR model can determine whether geopotential height anomalies at the base point influence geopotential height anomalies at other locations the following week, and vice versa.

[18] We consider three VAR models. One is unrestricted (U), meaning all coefficients in equations (6) and (7) are retained. Two are restricted; in restricted model R1 we impose $a_{12} = 0$, so that B_t does not depend on z_{t-1} (previous week’s value of geopotential height at the test location). In restricted model R2 we impose $a_{21} = 0$, so that z_t does not depend on B_{t-1} (previous week’s value of geopotential height at the base point). These three VAR models are summarized in Table 1.

[19] To test for Granger causality we introduce the test statistic L given by

$$L = (T - c)(\log|\Sigma_R| - \log|\Sigma_U|), \quad (8)$$

where T is again the number of weekly observations, $|\Sigma|$ is the determinant of the covariance matrix of residual errors in either the restricted (subscript R, model R1 or R2) or unrestricted model (subscript U) model, and $c = 2$ is the number of a_{ij} coefficients estimated in each equation of the unrestricted model U [*Enders*, 2004; *Sims*, 1980]. The test statistic L has an asymptotic χ^2 distribution with, in the case of a single lag, one degree of freedom. When testing for significance, the null hypothesis H_0 assumes the restricted model is sufficient to describe the system. Rejection of H_0 implies that the restricted model is insufficient, with de facto acceptance of the unrestricted model as an alternative. All statistical tests are performed at the 99% confidence level.

[20] For any given base point, the VAR model in equations (6) and (7) tests how strongly z at one location in the domain depends on B at the base point in the previous week, and vice versa. By fixing the base point and performing VAR model tests for z at every location throughout the domain, we are able to build a map, specific to our choice of base point for B , which indicates locations where $z \Rightarrow B$ and $B \Rightarrow z$.

3.5. Granger Density

[21] As will be shown later, it is useful to count how often z at a given location Granger causes B for a variety of choices of location of B throughout the domain. For example, some locations may exhibit $z \Rightarrow B$ for many base point choices (λ_B, ϕ_B) , whereas others may exhibit no Granger causality for any choice of base point (i.e., $z \not\Rightarrow B$ for all choices of (λ_B, ϕ_B)).

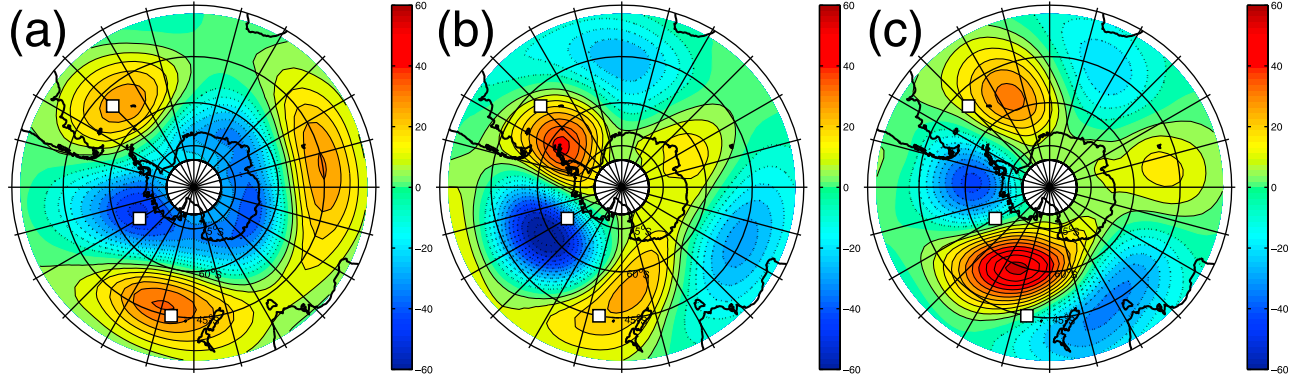


Figure 1. (a) First empirical orthogonal function (EOF) of 700 hPa geopotential height (z) in austral winter (July–August–September (JAS)). (b) Same as in Figure 1a, but for the second EOF. (c) Same as in Figure 1a, but for the third EOF. Contours are shown at intervals of 5 m, with the zero contour omitted. Positive contours are solid, and negative contours are dotted. White boxes mark the locations used when generating the *Yuan and Li* [2008] Pacific South American (PSA) index.

[22] To allow us to measure this, we first define a function of longitude and latitude which takes value 0 if $z \not\Rightarrow B$, or 1 if $z \Rightarrow B$, for a given choice of B which is located at (λ_B, ϕ_B) , that is

$$V(\lambda, \phi; \lambda_B, \phi_B) = \begin{cases} 1, & z(\lambda, \phi) \Rightarrow B(\lambda_B, \phi_B), \\ 0, & \text{otherwise.} \end{cases}$$

By considering a set of N_B distinct base points (λ_B, ϕ_B) , we then construct a “Granger density”, ρ_V , by summing V over our choice of base points

$$\rho_V(\lambda, \phi) = \frac{1}{N_B} \sum_{\lambda_B, \phi_B} V(\lambda, \phi; \lambda_B, \phi_B). \quad (9)$$

[23] High values of ρ_V denote regions where $z \Rightarrow B$ for many of the chosen base points, and low values denote regions where $z \Rightarrow B$ for very few of the chosen base points. The extrema $\rho_V = 1$ and $\rho_V = 0$ occur where $z \Rightarrow B$ for all base points and $z \Rightarrow B$ for none of the base points, respectively. Note that we only consider the Granger density for instances where $z \Rightarrow B$, i.e., testing model U against model R1. The opposite direction of Granger causality, $B \Rightarrow z$, is ignored for this purpose.

4. Results

4.1. EOF Analysis

[24] Results of the EOF analysis are shown in Figure 1. The leading mode, which is traditionally associated with the SAM, shows significant departure from an annular structure: negative anomalies which are situated over the pole in the standard SAM framework “spill out” equatorward in the Bellingshausen Sea region between 135°W – 90°W , forming a trough between two positive anomaly ridges that occur east of New Zealand and over the Weddell Sea, at approximately 180°W – 135°W and 60°W – 15°W , respectively. The locations of these positive and negative centers of action in EOF 1 coincide with the locations used for the *Yuan and Li* [2008] PSA index, which are marked in Figure 1 by white boxes. This Pacific sector peak-trough-peak pattern in z variability is echoed in EOFs 2 and 3, where it appears as the

most noticeable pattern of variability throughout the Southern Hemisphere. However, we note that the exact location of the peaks and troughs varies between EOFs 1, 2 and 3, giving rise to previous interpretations that these patterns represent interleaving wave-like patterns of variability in the Pacific sector [e.g., *Hobbs and Raphael*, 2010a; *Mo and Paegle*, 2001]. In some cases, these interleaving wave-like patterns in the Pacific sector have been defined using up to the first six EOF modes [e.g., *Kidson*, 1999].

[25] However, one must be careful when interpreting the results of EOF analysis in this way. First, the orthogonality requirement between EOF modes means that no individual mode is truly independent of other modes. This means that variability in z which is not explained by the peak-trough-peak pattern in the leading mode EOF, that is, variability lying between these peaks and troughs, will naturally be picked up by higher-order modes. Therefore, to some degree it is to be expected that interleaving patterns of variability will appear in higher-order EOF modes, irrespective of whether these patterns are truly dominant in the observed variability (see *Hannachi et al.* [2007] and *Monahan et al.* [2009] for further discussion). Second, higher-order modes are less likely to be distinct from one another. Figure 2 shows the separation criteria of [North et al., 1982] for the first 10 modes of our EOF analysis. Of the three modes shown in Figure 1 only the leading EOF mode, which describes just under 17% of the overall variability, is well separated from other modes. In fact, with the exception of EOF mode 6, none of the remaining modes are well separated from one another, meaning that their interpretation as independent modes of variability which interleave with one another is difficult to justify.

[26] These difficulties when interpreting our EOF results motivate using different methods to identify and describe variability of the large scale flow in the Pacific sector during austral winter.

4.2. Zonal and Meridional Winds

[27] To illustrate the difference in horizontal winds between austral winter and summer, we now compare the seasonally averaged magnitude of the weekly zonal

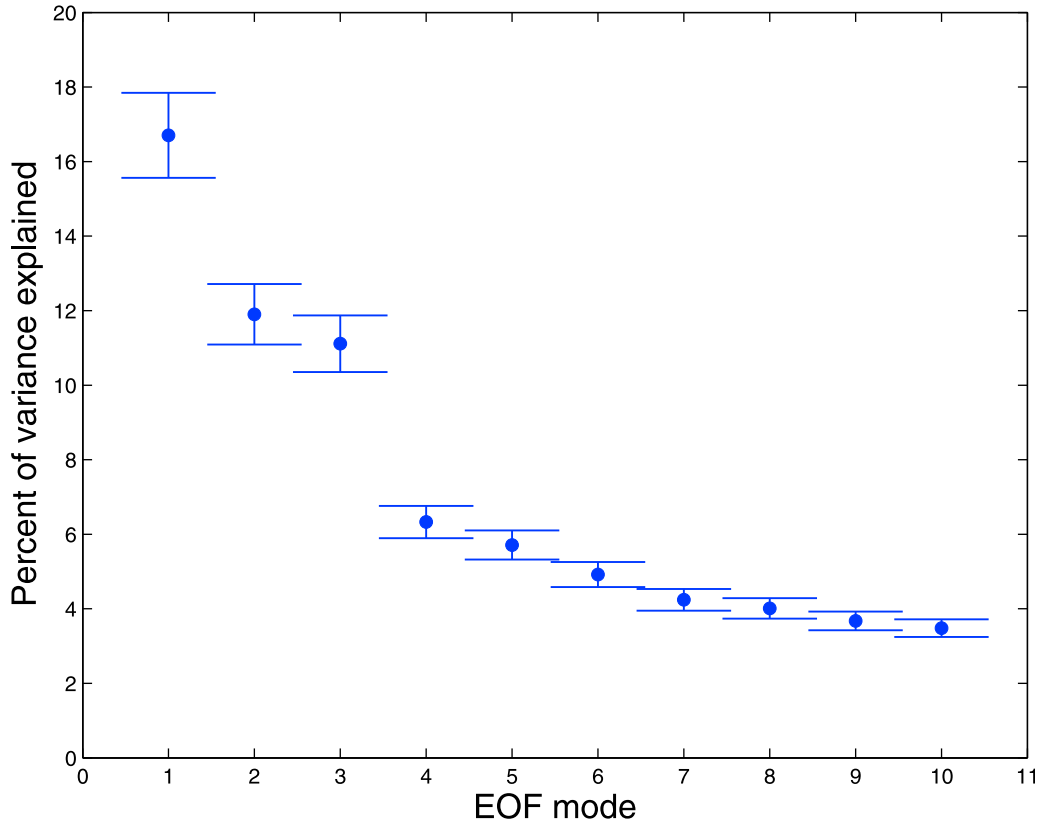


Figure 2. Percent of variance explained by the first 10 EOF modes of z variability in austral winter (JAS). Whisker plots denote the separation criteria of North *et al.* [1982].

wind, $\overline{|u|}_{\text{weekly}}^{\text{season}}$ (defined in (1)), and meridional wind, $\overline{|v|}_{\text{weekly}}^{\text{season}}$ (defined in (2)), between the two seasons. As the mean zonal flow is predominantly westerly in both seasons, the choice of $|u|$ rather than u when constructing the mean shown here makes no noticeable difference. However, in the case of the meridional wind, which is often both southerly and northerly during each season, our choice of $|v|$ rather than v avoids cancellation of large magnitude measurements which are of opposite sign.

[28] Our results are shown in Figure 3 and are similar to those discussed in previous studies [e.g., Chen *et al.*, 1996; Nakamura and Shimpo, 2004]. In austral summer (JFM) $\overline{|u|}_{\text{weekly}}^{\text{season}}$ has an annular structure, with larger amplitudes in the Eastern Hemisphere than in the Western Hemisphere. In contrast, during austral winter (JAS), $\overline{|u|}_{\text{weekly}}^{\text{season}}$ indicates that the zonal flow in the Western Hemisphere is significantly disrupted, leading to two quasi-zonal jets: the first located at approximately 60°S , and the second at approximately 30°S . Although not shown, despite its overall equivalent barotropic behavior, a degree of height dependence is observed in $\overline{|u|}_{\text{weekly}}^{\text{season}}$ during austral winter, with the subtropical jet in the Pacific sector increasing in strength with altitude. However, its bulk characteristics, that is its split jet structure and inherent zonal asymmetry compared to austral summer, still dominate at all heights. The seasonal mean of meridional wind magnitude, $\overline{|v|}_{\text{weekly}}^{\text{season}}$, is also seasonally and hemispherically dependent. In austral summer, contours have an almost annular structure, with higher magnitude in the Pacific sector. However, in austral winter, the annular

structure in $\overline{|v|}_{\text{weekly}}^{\text{season}}$ becomes much less apparent, with magnitudes in the western Southern Hemisphere being much larger than in austral summer.

4.3. Correlation Analysis

[29] Contours of the teleconnection function $\mathcal{T}(\lambda, \phi)$ are shown in Figure 4a for austral summer and in Figure 4b for winter. In summer, there are three main teleconnections. The strongest teleconnection occurs in the Pacific sector, with centers of action lying over the southeastern Pacific Ocean and South America. The next strongest teleconnection has centers over the Bellingshausen and Ross Seas, and New Zealand, and the last teleconnection has centers over the southern Indian Ocean and the portion of Antarctica lying in the Eastern Hemisphere.

[30] In the winter teleconnection map (Figure 4b), at middle to high latitudes we will focus on the three maxima which are located approximately over the Weddell Sea (center 7), the Bellingshausen Sea (center 2), and east of New Zealand (center 1), marked by white circles and numbers in Figure 4b. The location of these three centers closely matches the location of the peak-trough-peak pattern in the Pacific sector of the first EOF in Figure 1a. The location at which the strongest negative contemporaneous correlation occurs for each of these centers is marked by a blue circle, joined to the corresponding center by a blue line. We see that the Bellingshausen Sea and New Zealand teleconnection centers have a reciprocal relationship with one another, while the Weddell Sea teleconnection center is most strongly associated with a location slightly northeast of the Bellingshausen Sea center.

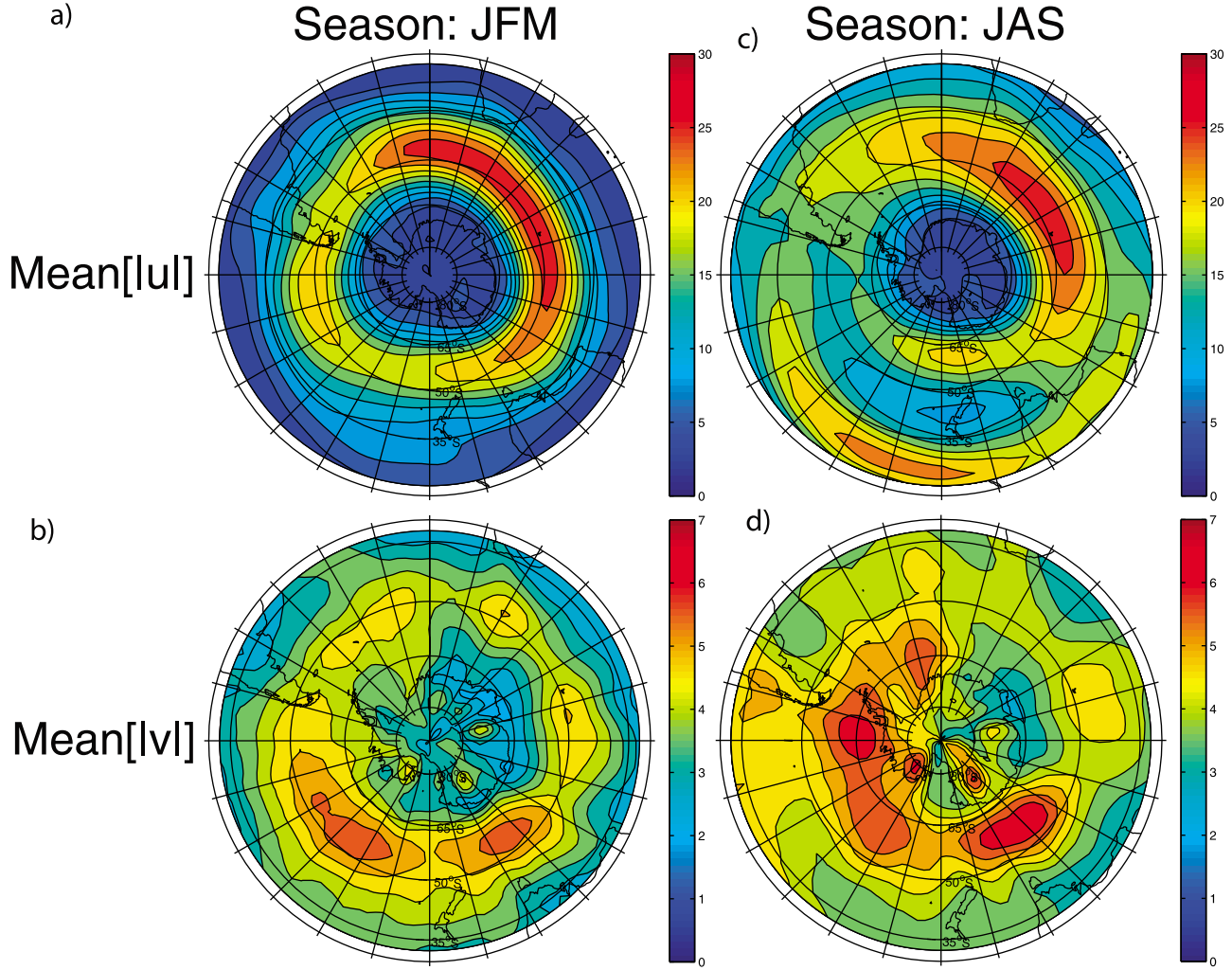


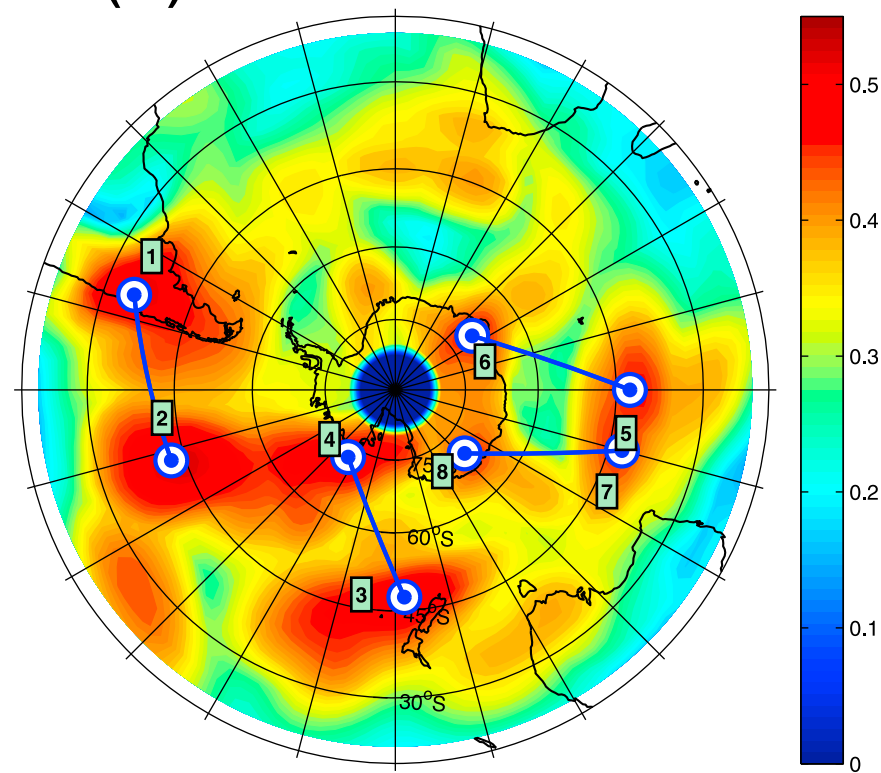
Figure 3. (a) The $\overline{|u(\lambda, \phi)|}_{\text{season}}$ at each point in the domain, averaged over January–February–March (JFM) in all years between 1978 and 2010. Contours are shown at intervals of 2.5 m s^{-1} . (b) The $\overline{|v(\lambda, \phi)|}_{\text{season}}$ at each point in the domain, averaged over JFM in all years between 1978 and 2010. Contours are shown at intervals of 0.5 m s^{-1} . (c) As in Figure 3a, but with averaging over JAS in all years between 1978 and 2010. (d) As in Figure 3b, but with averaging over JAS in all years between 1978 and 2010.

[31] To illustrate how sensitive these relationships are in space, we look at the location of strongest negative contemporaneous correlation for base points in the vicinity of these centers, as shown in Figure 5. For base point locations over the Weddell Sea (Figure 5a), their strongest teleconnection is with locations throughout the Bellingshausen Sea. Similarly, Figure 5c shows that base point locations in the vicinity of the New Zealand teleconnection center also have strongest teleconnection with locations over the Bellingshausen Sea. However, for base points lying over the Bellingshausen Sea region (Figure 5b), there are two distinct preferences for strongest teleconnection location: base points over the southern Bellingshausen Sea have strongest teleconnection with locations east of New Zealand, whereas

base points over the northeastern Bellingshausen Sea have strongest teleconnection with locations over the Weddell Sea. Because of this change in direction of teleconnection between the north and south Bellingshausen Sea, when defining a teleconnection center that is representative of the points in Figure 5b, it is useful to choose a location which is close to the center of the Bellingshausen Sea region. Such a choice is marked by a diamond in Figure 5b, and is seen in Figure 4b to be collocated with the location of strongest negative correlation for the Weddell Sea teleconnection center. While not corresponding to a peak in the teleconnection function in Figure 4b, z at this point correlates highly with z lying over both the New Zealand and Weddell Sea teleconnection centers, such that this choice of location

Figure 4. (a) Austral summer (JFM) teleconnection map $T(\lambda, \phi)$. White circles mark local minima in $T(\lambda, \phi)$. Blue lines connect each minima in $T(\lambda, \phi)$ with the location at which its strongest negative correlation occurs, marked by blue circles. Numbers represent the ordering of the minima, starting with 1 for the largest in magnitude. (b) As in Figure 4a, but for austral winter (JAS). The diamond in Figure 4b denotes the relocated Bellingshausen Sea teleconnection center (see text for details).

(a) Season: JFM



(b) Season: JAS

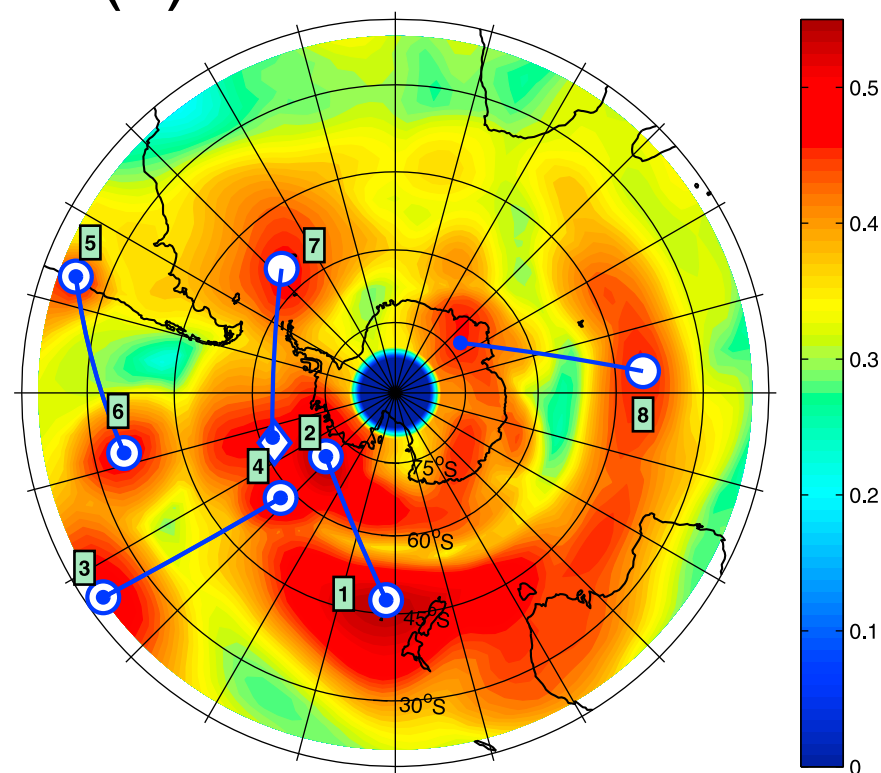
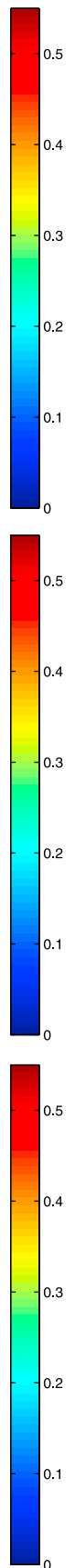
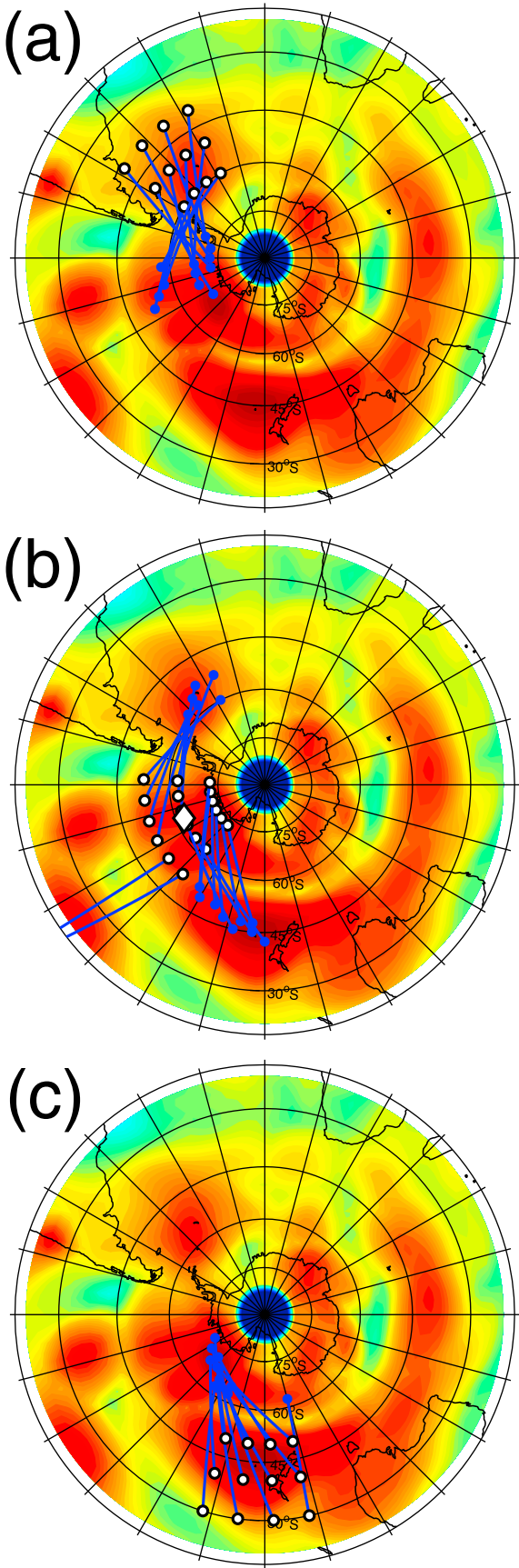


Figure 4



better represents a linkage between the three centers. In the remainder of this study, therefore, we will consider Western Hemisphere teleconnection centers located over the Weddell Sea at 55°S, 42.5°W; the Bellingshausen Sea at 62.5°S, 112.5°W; and east of New Zealand at 47.5°S, 178.5°W.

4.4. VAR Model Analysis of Teleconnection Centers

[32] The extent to which geopotential height anomalies at the Weddell Sea, Bellingshausen Sea, and New Zealand teleconnection centers influence, and are in turn influenced by, geopotential height anomalies elsewhere in the domain, is now tested using the VAR model framework introduced in section 3.4. The advantage of this analysis is that directions of Granger causality can be isolated, giving an indication of “upstream” and “downstream” dependencies.

[33] Figure 6 shows VAR model results when using the Weddell Sea (Figures 6a and 6b), Bellingshausen Sea (Figures 6c and 6d), and New Zealand (Figures 6e and 6f) teleconnection centers for the base point time series B used in equations (6) and (7). In addition to these three centers of action, the original Bellingshausen Sea and Indian Ocean teleconnection centers are marked for completeness.

[34] The VAR model is fit independently for z at every point in the domain, giving spatial maps of VAR model test results for each choice of base point. Figures 6a, 6c, and 6e show results for unrestricted VAR model U tested against restricted VAR model $R1$ (i.e., fully coupled, versus B independent of z), and Figures 6b, 6d, and 6f show results for unrestricted model U tested against restricted VAR model $R2$ (i.e., fully coupled, versus z independent of B). The light shading in Figure 6a indicates regions where z Granger causes the Weddell Sea B ($z \Rightarrow B$), that is, regions where z is significant in determining geopotential height anomalies at the Weddell Sea base point in the following week. Similarly, dark shading in Figure 6b indicates regions where the Weddell Sea B Granger causes z ($B \Rightarrow z$), that is, regions in which geopotential height anomalies depend significantly on what is happening at the Weddell Sea base point in the previous week.

[35] In general, Figures 6a, 6c, and 6e indicate that geopotential height anomalies at these base points have significant lagged dependence on z lying to the west, or upstream, given the climatological westerly zonal flow. Similarly, Figures 6b, 6d, and 6f indicate that the dependence on the base point in following weeks is generally confined to locations lying to the east, or downstream. We note that none of the plots in Figure 6 indicate “annular mode” characteristics. Furthermore, although not shown here, annular mode characteristics were not identified at all when using a wide range of alternative base points in the VAR model.

[36] Overall, the Granger causality picture presented here is one of a wave-like eastward propagation of information:

Figure 5. The same as Figure 4, but showing the location of strongest negative correlation for points in the vicinity of minima (a) 7, (b) 2, and (c) 1 in $\mathcal{T}(\lambda, \phi)$ shown in Figure 4b (JAS). The diamond in Figure 5b denotes the relocated Bellingshausen Sea teleconnection center (see text for details).

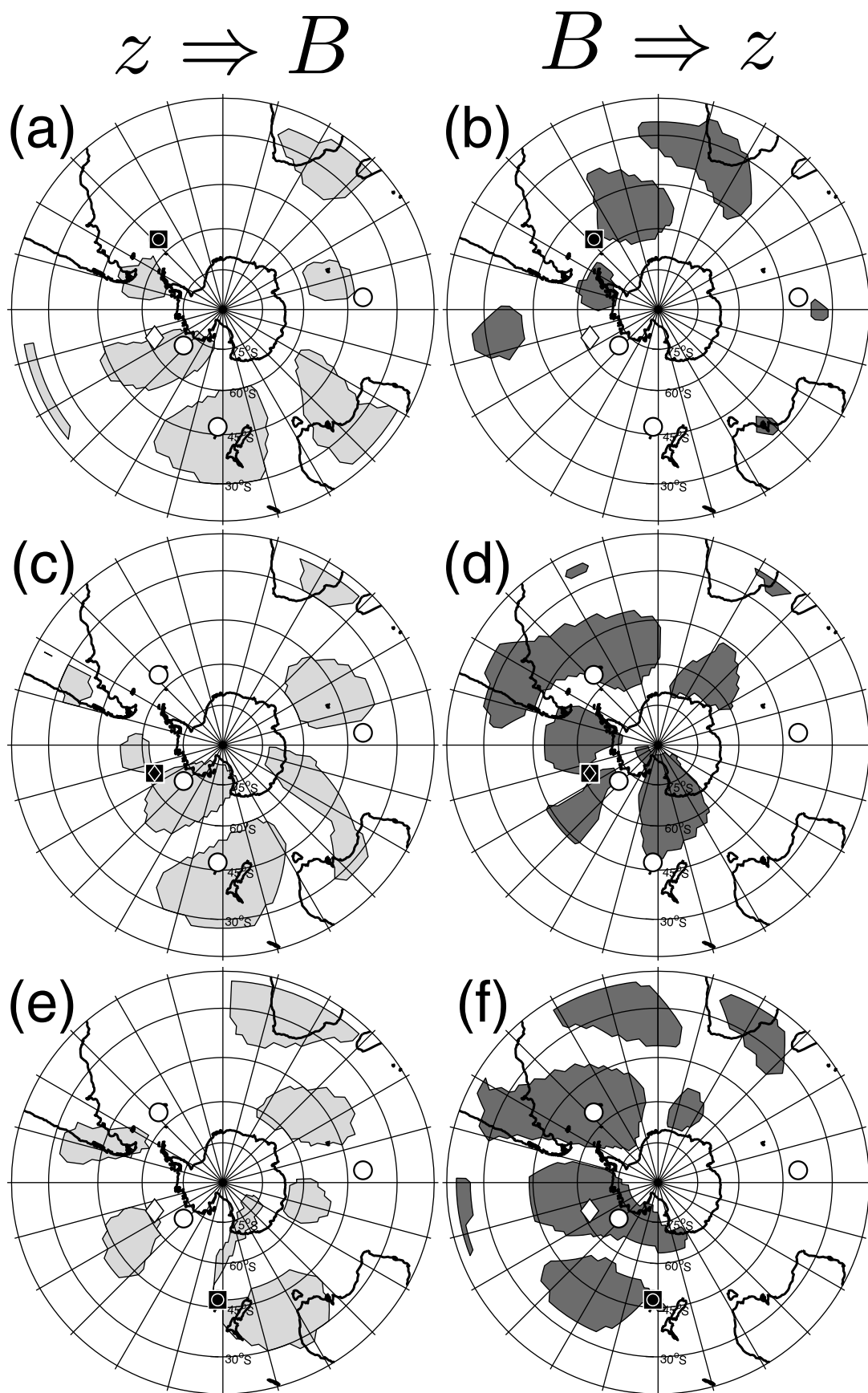


Figure 6

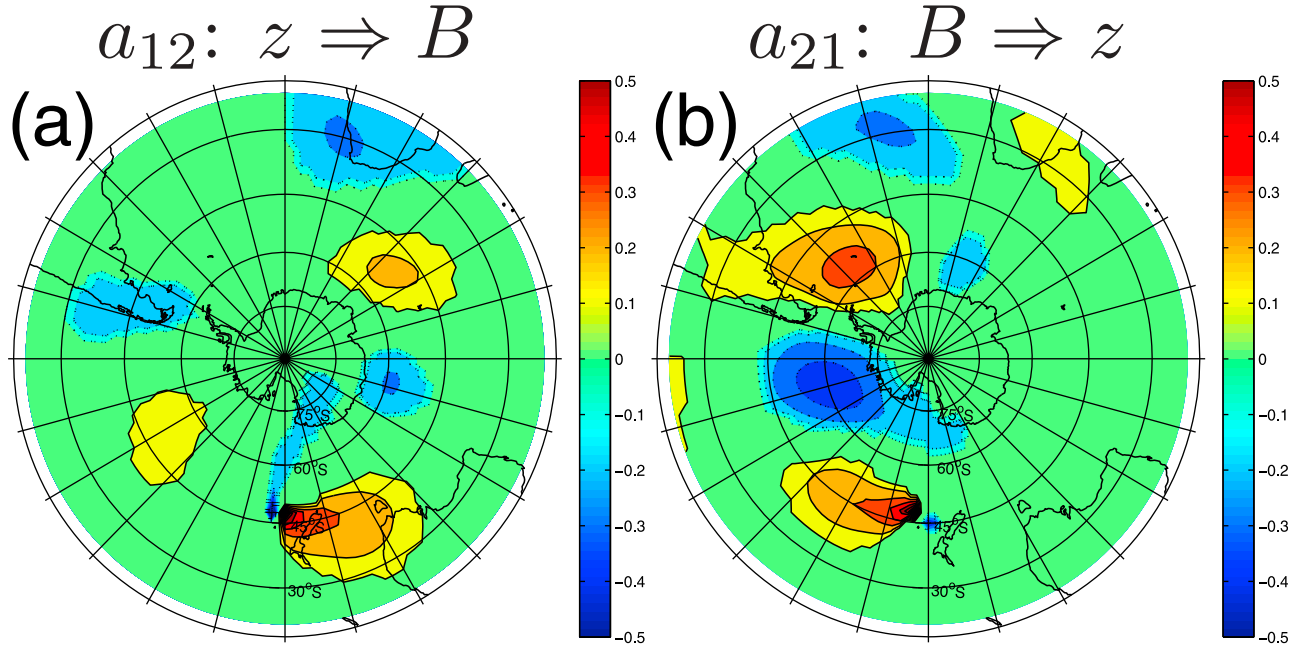


Figure 7. (a) Magnitude of a_{12} in the unrestricted model U when B is taken to be located over the austral winter New Zealand teleconnection center, as shown in Figure 4b (JAS). Only regions in which a_{12} is statistical significant at the 99% level, as shown in Figure 6e, are contoured. (b) As in Figure 7a, but for a_{21} , with shaded regions in Figure 6f being contoured. The contour interval in both plots is 0.1, with dotted contours denoting negative values.

geopotential height anomalies at each base point are generally influenced by anomalies lying upstream (to the west) in the previous week, and in turn influence anomalies lying downstream (to the east) in the following week. Variation in the propagation of information between the Pacific, Atlantic and Indian Ocean sectors can be deduced by looking at the magnitude of the a_{ij} coefficients in the VAR model (see equations (6) and (7)). When considering B located over the New Zealand teleconnection center, as shown in Figure 7 (see also Figures 6e and 6f), we see that the magnitude of a_{21} in the Pacific and Atlantic sectors is larger than a_{12} in the Indian Ocean sector, indicating that geopotential height anomalies at the New Zealand teleconnection center (B) are most strongly coupled with z lying in the western Southern Hemisphere, or downstream. The New Zealand center is chosen as it is located at the cusp of the Pacific and Indian Ocean, and might therefore be expected to have a_{ij} of similar magnitude in both sectors, although this is clearly not the case.

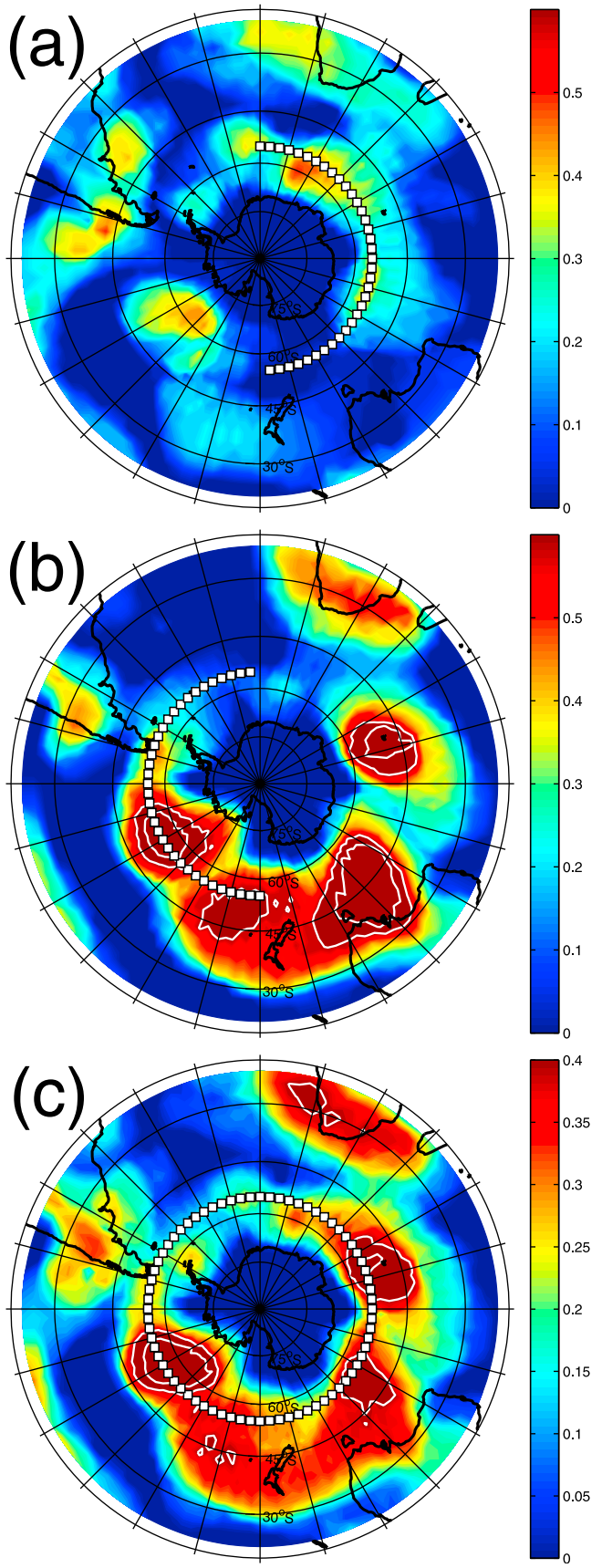
4.5. Granger Density

[37] One remaining question surrounding the VAR model maps in Figure 6 is the sensitivity of these maps to the

choice of base point, and the influence of eastward advection of disturbances by the background flow, rather than wave propagation. For example, should the base point in Figure 6a be moved 15° to the west, would the map of VAR model results also relocate 15° to the west, while retaining a similar distribution? Such a result would be evidence of eastward advection of geopotential height disturbances. However, should the pattern of VAR model results remain largely stationary despite a relocation of the base point, we would have evidence of a quasi-stationary wave. To this end, we now present Granger density ρ_V results, where the summation in equation (9) is over base points taken at 5° longitude intervals around the 55°S zonal circle, with a separate calculation for ρ_V for each choice of base points.

[38] The Granger density, ρ_V , is interpreted in the following way. If the regions where $z \Rightarrow B$ (denoted by light shading in Figure 6) are due to advection of geopotential height anomalies by the mean westerly zonal wind, then if the chosen base point is relocated in the zonal direction, one would expect the pattern of light shading to be similarly relocated while retaining its bulk characteristics. Therefore, when averaging over a set of zonally distributed base points to generate ρ_V , this would result in the ρ_V being

Figure 6. Maps of vector autoregressive model test results when using base point time series B located over (a and b) the Weddell Sea, (c and d) Bellingshausen Sea, and (e and f) New Zealand teleconnection centers. In Figures 6a, 6c, and 6e, light shading denotes regions where fully coupled model U is a significantly better fit to observed data than restricted model R1 (i.e., $z \Rightarrow B$, such that B is lag dependent on z). In Figures 6b, 6 d, and 6f, dark shading denotes regions where fully coupled model U is a significantly better fit to observed data than restricted model R2 (i.e., $B \Rightarrow z$, such that z is lag dependent on B). All tests are performed at the 99% confidence level. White circles denote teleconnection centers 1, 2, 7, and 8 from Figure 4b (JAS), the diamond denotes the relocated Bellingshausen Sea teleconnection center (see text for details), and the shaded boxed symbol denotes the base point location for each plot.



approximately uniformly distributed. However, if the occurrence of $z \Rightarrow B$ in Figure 6 is due to a quasi-stationary teleconnection wave pattern, rather than advection of anomalies, we might expect the light shading to remain in place, even once the base point is moved. This behavior would be observed in ρ_V as a collection of peaks and troughs, as opposed to the approximately uniform distribution described above for the anomaly advection scenario.

[39] Figure 8 shows maps of $\rho_V(\lambda, \phi)$ created using three sets of base points lying at 5° longitude intervals around the 55°S zonal circle: Eastern Hemisphere $0^\circ \leq \lambda < 180^\circ$ (Figure 8a), Western Hemisphere $180^\circ \leq \lambda < 360^\circ$ (Figure 8b), and both hemispheres $0^\circ \leq \lambda < 360^\circ$ (Figure 8c), with the chosen base points marked by white squares. Large $\rho_V(\lambda, \phi)$ denotes regions where $z \Rightarrow B$ at many of the chosen base points. Small $\rho_V(\lambda, \phi)$ denotes regions where $z \Rightarrow B$ for few, if any, of the chosen base points. We note, however, that we are primarily interested in the uniformity of the $\rho_V(\lambda, \phi)$ distribution, rather than its exact magnitude.

[40] For base points lying on the 55°S zonal circle in the Eastern Hemisphere, as shown in Figure 8a, the Granger density is nonuniform, exhibiting two distinct peaks at middle to high latitudes. The first peak is over the Bellingshausen Sea, and the second is over the Indian Ocean south of Africa. The magnitude of ρ_V exceeds 0.4 in both cases, indicating that geopotential height anomalies over these regions Granger cause geopotential height anomalies at approximately 40% of the chosen base points.

[41] When considering base points lying in the Western Hemisphere, as shown in Figure 8b, the ρ_V distribution is different to that seen in the Eastern Hemisphere, but is also nonuniform. There are five distinct peaks in the Granger density, located over the Bellingshausen Sea, east of New Zealand, south of Australia, in the southern Indian Ocean, and over South Africa. These peaks remain easily distinguishable when considering base points lying in both hemispheres, as shown in Figure 8c, and approximately match locations where Granger causality is observed in Figures 6a, 6c, and 6e. This indicates that dependency of anomalies between these regions is due to a quasi-stationary teleconnection wave pattern, rather than eastward advection of anomalies by the background zonal flow.

[42] Although differences exist between Figures 8a and 8b, there are some notable common features in their $\rho_V(\lambda, \phi)$ distributions. First, geopotential height anomalies lying over the Bellingshausen Sea are significant when determining anomalies at 55°S in both hemispheres the following week. Secondly, the small peak in $\rho_V(\lambda, \phi)$ lying over the eastern

Figure 8. (a) Contours of ρ_V when using base points lying at 5° intervals around the 55°S zonal circle in the Eastern Hemisphere ($0^\circ \leq \lambda < 180^\circ$). (b) As in Figure 8a, but for the Western Hemisphere ($180^\circ \leq \lambda < 360^\circ$). (c) As in Figure 8a, but for base points spanning both hemispheres ($0^\circ \leq \lambda < 360^\circ$). The chosen base points are denoted by white squares in all plots. In Figures 8a and 8b, contours are shown at an interval of 0.01 for $\rho_V \leq 0.6$ (shaded) and 0.10 for $\rho_V \geq 0.6$ (white). In Figure 8c, contours are shown at an interval of 0.01 for $\rho_V \leq 0.4$ (shaded) and 0.10 for $\rho_V \geq 0.4$ (white).

Weddell Sea in Figure 8a is much smaller than any of the peaks described above, and is almost indistinguishable when considering both hemispheres together (Figure 8c). This suggests that while this teleconnection center receives information from teleconnection centers lying upstream (e.g., the Bellingshausen Sea and New Zealand teleconnection centers, as shown in Figure 6a), it does not effectively transmit information to downstream locations in the Eastern Hemisphere at 55°S. Finally, and most importantly, the peak-trough-peak pattern in $\rho_1(\lambda, \phi)$ in Figure 8c is primarily associated with base points lying in the Western Hemisphere (see Figure 8b), which indicates that the teleconnection centers which exist in this sector, namely the New Zealand, Bellingshausen Sea and Weddell Sea centers, are associated with quasi-stationary wave behavior. In addition, it is seen that none of the base points in either hemisphere exhibit dependence on geopotential height anomalies occurring over the Antarctic continent, a location which is important when considering the annular mode paradigm.

5. Conclusions

[43] This study has applied a range of techniques to investigate ambiguity in Southern Hemisphere climate modes during austral winter, using weekly average data. A weekly time scale is appropriate considering the short decorrelation time scale of intraseasonal atmospheric anomalies. The techniques we have used include EOF analysis, correlation-teleconnection analysis, and novel application of a VAR model framework to test for directions of causality. Although we focus on austral winter we also use these techniques on atmospheric fields during austral summer, which are known to exhibit strong annular mode characteristics, to allow contrast and comparison between the two seasons.

[44] The main findings of our study are summarized as follows.

[45] 1. As noted in previous studies [e.g., *Chen et al.*, 1996], in contrast to austral summer, the background flow during austral winter shows significant asymmetry between the Eastern and Western Hemispheres. Although zonal flow dominates in both instances, it is much more disrupted in the Western Hemisphere during austral winter, where it exhibits a split jet structure (see Figure 3).

[46] 2. Utilizing a correlation analysis approach, we show that weaker zonal flow in the Western Hemisphere during winter is characterized by three teleconnection centers, located approximately over the Weddell Sea, the Bellingshausen Sea, and east of New Zealand, as shown in Figure 4b. The relationship between the three is as follows: the north Bellingshausen Sea communicates with the Weddell Sea teleconnection center, and the south Bellingshausen Sea communicates with the New Zealand teleconnection center (see Figure 5). These three locations coincide with centers of action in two existing definitions of Southern Hemisphere climate modes: the SAM, defined using the 1st EOF of 700 hPa geopotential height anomalies (see Figure 1), and the fixed base point definition of the PSA (see the white boxes in Figure 1 of *Yuan and Li* [2008]). It was therefore necessary to investigate whether the behavior associated with these teleconnection centers is indicative of an annular (e.g., SAM), or nonannular (e.g., PSA) view of Southern Hemisphere climate variability.

[47] 3. Adopting a VAR model approach, the relationship between these teleconnection centers and geopotential height anomalies on the 700 hPa pressure surface is shown to exhibit predominantly wave-like characteristics (see Figure 6). This nonannular wave-like pattern during austral winter, which encompasses the Weddell Sea, Bellingshausen Sea, New Zealand teleconnection centers in the Western Hemisphere, with somewhat weaker centers of action in the Eastern Hemisphere over the southern Indian Ocean and the tip of South Africa, is quasi-stationary, and associated with eastward propagation of information.

[48] Overall, our results indicate that the leading mode of variability in the Southern Hemisphere during austral winter does not exhibit strong annular characteristics, in contrast to that during austral summer. Austral winter variability is dominated by a quasi-stationary wave pattern which has largest magnitude in the Western Hemisphere, suggesting that it is best to think of intraseasonal variability in this region in terms of wave-like teleconnection patterns, for example the PSA, rather than as the Western Hemisphere portion of the wintertime SAM. This provides an argument against resorting to 2nd, 3rd and higher EOF modes, which are often not distinct from one another, to define the PSA pattern in winter. Rather, the wave-like pattern, not the annular pattern, should be considered the dominant climate mode, especially in the western Southern Hemisphere.

[49] The question remains as to why the leading mode of variability in austral winter is wave-like, in contrast to the annular mode variability during summer? One possible reason is the interaction of midlatitude Rossby waves with the mean flow during each season. That is, the split jet in the western Southern Hemisphere during austral winter leads to less focused (or more widespread) Rossby wave breaking, compared to the single jet structure during austral summer which leads to Rossby wave breaking occurring over a more localized region [*Wang and Magnusdottir*, 2011]. This focused Rossby wave breaking during summer then drives a coherent north-south seesaw pattern in geopotential height variability, which in turn reinforces the single jet mean flow structure.

[50] Also, although our results suggest that the leading mode of variability is wave-like, it is difficult to detect the possibility, and extent, to which Rossby wave patterns of different time scales and dynamical sources interfere with one another. For example, it is possible that the large amplitude of the wave pattern in the Western Hemisphere is due to constructive interference of a circumpolar quasi-stationary Rossby wave with a quasi-stationary Rossby wave which is excited by Pacific tropical forcing and localized to the South Pacific–Bellingshausen Sea–South Atlantic region (a discussion of the coexistence and interaction of different Rossby waveforms in this way is given by *Karoly* [1989], *Karoly et al.* [1989], and *Carleton* [2003]). Although not shown, some evidence of this is observed by repeating our geopotential height teleconnection analysis using only winters occurring during El Niño episodes (defined using the Oceanic Niño Index obtained from <http://www.cpc.ncep.noaa.gov>). In this instance, teleconnection between the tropical Pacific and the Bellingshausen Sea dominates. That is, reciprocating centers 3 and 4 in Figure 4b dominate during El Niño episodes, suggesting the enhanced role of tropically

forced Rossby waves during these winters. Further exploration of this possibility is left to further study.

[51] Nevertheless, the unsuitability of the annular mode paradigm when describing austral winter variability remains clear, and it is our intention that this study will help clarify any ongoing ambiguity in the definition of annular versus wave-like climate modes during austral winter. Clarification of such ambiguity is essential if one is to consider interaction between these modes and other elements of the climate system.

Appendix A: VAR Model Details

[52] The VAR model in (6) and (7) can be expressed in vector form as

$$\begin{pmatrix} B_t \\ z_t \end{pmatrix} = \begin{pmatrix} a_{11} & a_{12} \\ a_{21} & a_{22} \end{pmatrix} \begin{pmatrix} B_{t-1} \\ z_{t-1} \end{pmatrix} + \begin{pmatrix} \epsilon_t^B \\ \epsilon_t^z \end{pmatrix}. \quad (\text{A1})$$

Parameters a_{ij} are estimated by fitting (A1) to observed B_t and z_t time series with residual errors $(\epsilon_t^B, \epsilon_t^z)$ replacing stochastic forcing terms $(\epsilon_t^B, \epsilon_t^z)$. When fitting the model, the left hand side of (A1) uses B_t and z_t values for weeks starting 1 January up to 26 March for austral summer, and 2 July up to 24 September for austral winter, with the weeks preceding these periods being used for lagged values on the right hand side where necessary. The remaining two unknown parameters in the system, variances σ_B^2 and σ_z^2 of the stochastic forcing terms, are given by the covariance matrix constructed using the residual error terms

$$\Sigma = \begin{pmatrix} \text{var}(\epsilon_t^B) & \text{cov}(\epsilon_t^B, \epsilon_t^z) \\ \text{cov}(\epsilon_t^B, \epsilon_t^z) & \text{var}(\epsilon_t^z) \end{pmatrix}, \quad (\text{A2})$$

where $\sigma_B^2 = \text{var}(\epsilon_t^B) = \text{var}(\epsilon_t^z)$ and $\sigma_z^2 = \text{var}(\epsilon_t^z) = \text{var}(\epsilon_t^B)$.

[53] As we impose asymmetrical restrictions on these lagged dependencies (e.g., $a_{12} \equiv 0$ in model R1 in section 4.4, meaning z_t depends on both B_{t-1} and z_{t-1} , whereas B_t depends only on its previous value B_{t-1}), it is statistically efficient to fit the model to observed data using seemingly unrelated regression (SUR) rather than ordinary least squares regression (OLS) [Enders, 2004; Zellner, 1962]. The SUR method is similar to that of OLS and is omitted here in the interest of brevity. However, we note that when B_t and z_t have exactly the same number of lagged dependencies, as seen in model U in section 4.4 for example, parameter estimates using SUR and OLS are identical.

[54] **Acknowledgments.** This work was supported by NOAA grant NA09OAR4310132. The authors would like to thank Hal Stern for helpful suggestions concerning implementation of the VAR model framework. They thank Xiaojun Yuan and an anonymous reviewer for helpful comments on the paper.

References

- Amabaum, M. H. P., B. J. Hoskins, and D. B. Stephenson (2001), Arctic Oscillation or North Atlantic Oscillation?, *J. Clim.*, 14, 3495–3507.
- Ambrizzi, T., B. J. Hoskins, and H.-H. Hsu (1995), Rossby wave propagation and teleconnection patterns in the austral winter, *J. Atmos. Sci.*, 52, 3661–3672.
- Berbery, E. H., J. Nogués-Paegle, and J. D. Horel (1992), Wavelike Southern Hemisphere extratropical teleconnections, *J. Atmos. Sci.*, 49, 155–177.
- Bromwich, D. H., and R. L. Fogt (2004), Strong trends in the skill of the ERA-40 and NCEP-NCAR reanalyses in high and midlatitudes in the Southern Hemisphere, 1958–2001, *J. Clim.*, 17, 4603–4619.
- Carleton, A. M. (2003), Atmospheric teleconnections involving the Southern Ocean, *J. Geophys. Res.*, 108(C4), 8080, doi:10.1029/2000JC000379.
- Chen, B., S. R. Smith, and D. H. Bromwich (1996), Evolution of the tropospheric split jet over the South Pacific Ocean during the 1986–89 ENSO Cycle, *Mon. Weather Rev.*, 124, 1711–1731.
- Cohen, J., and K. Saito (2002), A test for annular modes, *J. Clim.*, 15, 2537–2546.
- Enders, W. (2004), *Applied Econometric Time Series*, 2nd ed., 466 pp., John Wiley, Hoboken, N. J.
- Frederiksen, C. S., and X. Zheng (2007), Variability of seasonal-mean fields arising from intraseasonal variability. Part 3: Application to SH winter and summer circulations, *Clim. Dyn.*, 28, 849–866.
- Gong, D., and S. Wang (1999), Definition of Antarctic oscillation index, *Geophys. Res. Lett.*, 26, 459–462.
- Granger, C. W. J. (1969), Investigating causal relationships by econometric models and cross spectral methods, *Econometrica*, 37, 424–438.
- Hannachi, A., I. T. Jolliffe, and D. B. Stephenson (2007), Empirical orthogonal functions and related techniques in atmospheric science: A review, *Int. J. Climatol.*, 27, 1119–1152.
- Hendon, H. H., D. W. J. Thompson, and M. C. Wheeler (2007), Australian rainfall and surface temperature variations associated with the Southern Hemisphere annular mode, *J. Clim.*, 20, 2452–2467.
- Hobbs, W. R., and M. N. Raphael (2010a), Characterizing the zonally asymmetric component of the SH circulation, *Clim. Dyn.*, 35, 859–873.
- Hobbs, W. R., and M. N. Raphael (2010b), The Pacific zonal asymmetry and its influence on Southern Hemisphere sea ice variability, *Antarct. Sci.*, 22, 559–571.
- Karoly, D. J. (1989), Southern Hemisphere circulation features associated with El Niño–Southern Oscillation events, *J. Clim.*, 2, 1239–1252.
- Karoly, D. J., R. A. Plumb, and M. Ting (1989), Examples of the horizontal propagation of quasi-stationary waves, *J. Atmos. Sci.*, 46, 2802–2811.
- Kidson, J. W. (1999), Principal modes of Southern Hemisphere low-frequency variability obtained from NCEP–NCAR reanalyses, *J. Clim.*, 12, 2808–2830.
- Matthewman, N. J., and G. Magnusdottir (2011), Observed interaction between Pacific sea ice and the western Pacific pattern on intraseasonal time scales, *J. Clim.*, 24, 5031–5042.
- Mo, K. C., and J. N. Paegle (2001), The Pacific–South American modes and their downstream effects, *Int. J. Climatol.*, 21, 1211–1229.
- Monahan, A. H., J. C. Fyfe, M. H. P. Amabaum, D. B. Stephenson, and G. R. North (2009), Empirical orthogonal functions: The medium is the message, *J. Clim.*, 22, 6501–6514.
- Mosedale, T. J., D. B. Stephenson, M. Collins, and T. C. Mills (2006), Granger causality of coupled climate processes: Ocean feedback on the North Atlantic Oscillation, *J. Clim.*, 19, 1182–1194.
- Nakamura, H., and A. Shimpo (2004), Seasonal variations in the Southern Hemisphere storm tracks and jet streams as revealed in a reanalysis dataset, *J. Clim.*, 17, 1828–1844.
- North, G. R., T. L. Bell, R. F. Cahalan, and F. J. Moeng (1982), Sampling errors in the estimation of empirical orthogonal functions, *Mon. Weather Rev.*, 110, 699–706.
- Sims, C. A. (1980), Macroeconomics and reality, *Econometrica*, 48, 1–48.
- Strong, C., G. Magnusdottir, and H. Stern (2009), Observed feedback between winter sea ice and the North Atlantic Oscillation, *J. Clim.*, 22, 6021–6032.
- Thompson, D. W. J., and J. M. Wallace (1998), The Arctic Oscillation signature in the wintertime geopotential height and temperature fields, *Geophys. Res. Lett.*, 25, 1297–1300.
- Wallace, J. M., and D. S. Gutzler (1981), Teleconnections in the geopotential height field during the Northern Hemisphere winter, *Mon. Weather Rev.*, 109, 784–812.
- Wang, Y.-H., and G. Magnusdottir (2011), Tropospheric Rossby wave breaking and the SAM, *J. Clim.*, 24, 2134–2146.
- Yuan, X., and C. Li (2008), Climate modes in southern high latitudes and their impacts on Antarctic sea ice, *J. Geophys. Res.*, 113, C06S91, doi:10.1029/2006JC004067.
- Zellner, A. (1962), An efficient method of estimating seemingly unrelated regressions and tests for aggregation bias, *J. Am. Stat. Assoc.*, 57, 348–368.

G. Magnusdottir and N. J. Matthewman, Department of Earth System Science, University of California, Irvine, CA 92697-3100, USA. (gudrun@uci.edu)